ing interactions that can be described essentially as two π-bonds (Fig. 1, right). Those MOs are localized slightly more on oxygen than on boron, reflecting the polar nature of this interaction. Additionally, they show substantial stabilizing contributions of the symmetry-equivalent d-orbitals of platinum.

Further evidence for the remarkable stability of the oxoboryl moiety in the coordination sphere of platinum was the clean reaction of **2** with $[Bu_4N]SPh$ (Ph being phenyl), as was evinced by means of NMR spectroscopy. The product features spectroscopic parameters very similar to those of the starting complex, and in particular IR data (1849 and 1793 cm^{-1}) indicate only minor influence of the *trans* ligand substitution on the oxoboryl moiety. As evidenced with x-ray analyses, the thiolate anion does not affect the boron center but instead reacts through substitution of the bromide ligand, yielding *trans*-$[(Cy_3P)_2(PhS)Pt(BO)]$ (**3**) (Scheme 2), which could be isolated in 62% yield.

The solid structure of **3** (Fig. 2) exhibits an almost square-planar geometry at platinum (sum of bond angles of 359.1°); however, the phosphine ligands are bent slightly toward the oxoboryl moiety [$<_{\mathrm{B-Pt-P}}$ = 87.75(8) and 86.80(8)°, respectively, the numbers in parentheses being the estimated SD]. The latter is coordinated to platinum terminally via the boron atom [$<_{\mathrm{Pt-B-O}}$ = 177.3(2)°], reflecting its sp-hybridization. The Pt–B distance [198.3(3) pm] is slightly longer than in the corresponding iminoboryl complex *trans*-$[(Cy_3P)_2(Br)Pt(BNSiMe_3)]$ [196.0(3) pm] (*27*, *28*) but in the typical range of classical boryl complexes of platinum with trivalent boron atoms *trans* to a bromide [196.3(6)–209.(3) pm] (*35*). The B–O bond length of 121.0(3) pm in **3** is slightly smaller than the value obtained for **2′** from DFT calculations and statistically indistinguishable from the distance calculated from microwave data of gaseous HBO [120.04(3) pm] (*11*). However, it is considerably smaller than the B–O double bond in the coordinated XBO [130.4(2) pm] (*26*). The observed bond shortening of 7.2% is only slightly smaller than the corresponding difference between alkynes and alkenes (9.9%) (*37*), providing further evidence of the presence of a triple bond between boron and oxygen.

Our approach of generating unusual ligand systems in the coordination sphere of transition metals has enabled us to access the previously elusive boron monoxide moiety. In marked contrast to main group–substituted XBOs, which are high-energy intermediates, compound **2** exhibits a remarkable thermal and light stability. Despite the stabilizing effect that the platinum fragment exerts on the oxoboryl moiety, we realized interesting reaction chemistry on both the BO ligand itself and on the metal center. Hence, the bromide ligand undergoes clean metathesis with the thiophenolate anion, leaving the BO ligand intact, whereas trimethyl(bromo)silane adds reversibly to the BO ligand. We anticipate a diverse range of further reactivity along both lines.

References and Notes

1. W. N. Lipscomb, *Science* **196**, 1047 (1977).
2. H. C. Brown, *Science* **210**, 485 (1980).
3. P. Paetzold, *Adv. Inorg. Chem.* **31**, 123 (1987).
4. A. Berndt, *Angew. Chem.* **105**, 1034 (1993).
5. A. Berndt, *Angew. Chem. Int. Ed. Engl.* **32**, 985 (1993).
6. W. E. Piers, S. C. Bourke, K. D. Conroy, *Angew. Chem.* **117**, 5142 (2005).
7. W. E. Piers, S. C. Bourke, K. D. Conroy, *Angew. Chem. Int. Ed.* **44**, 5016 (2005).
8. H. Braunschweig, C. Kollann, F. Seeler, *Struct. Bonding* **130**, 1 (2008).
9. L. Barton, F. A. Grimm, R. F. Porter, *Inorg. Chem.* **5**, 2076 (1966).
10. D. L. Hildenbrand, L. P. Theard, A. M. Saul, *J. Chem. Phys.* **39**, 1973 (1963).
11. Y. Kawashima, Y. Endo, K. Kawaguchi, E. Hirota, *Chem. Phys. Lett.* **135**, 441 (1987).
12. H. Bock *et al.*, *Angew. Chem.* **101**, 77 (1989).
13. H. Bock *et al.*, *Angew. Chem. Int. Ed. Engl.* **28**, 88 (1989).
14. E. R. Lory, R. F. Porter, *J. Am. Chem. Soc.* **93**, 6301 (1971).
15. A. Snelson, *High Temp. Sci.* **4**, 318 (1972).
16. A. Snelson, *High Temp. Sci.* **4**, 141 (1972).
17. L. Andrews, T. R. Burkholder, *J. Phys. Chem.* **95**, 8554 (1991).
18. D. V. Lanzisera, L. Andrews, *J. Phys. Chem. A* **101**, 1482 (1997).
19. H. F. Bettinger, *Organometallics* **26**, 6263 (2007).
20. B. Pachaly, R. West, *J. Am. Chem. Soc.* **107**, 2987 (1985).
21. P. Paetzold, S. Neyses, L. Geret, *Z. Anorg. Allg. Chem.* **621**, 732 (1995).
22. M. Ito, N. Tokitoh, R. Okazaki, *Tetrahedron Lett.* **38**, 4451 (1997).
23. P. Paetzold, P. Bohm, A. Richter, E. Scholl, *Z. Naturforsch. B* **31B**, 754 (1976).
24. A. Sekiguchi, R. Kinjo, M. Ichinohe, *Science* **305**, 1755 (2004).
25. M. Groteklaes, P. Paetzold, *Chem. Ber.* **121**, 809 (1988).
26. D. Vidovic, J. A. Moore, J. N. Jones, A. H. Cowley, *J. Am. Chem. Soc.* **127**, 4566 (2005).
27. H. Braunschweig, K. Radacki, D. Rais, K. Uttinger, *Angew. Chem.* **118**, 169 (2006).
28. H. Braunschweig, K. Radacki, D. Rais, K. Uttinger, *Angew. Chem. Int. Ed.* **45**, 162 (2006).
29. H. Braunschweig *et al.*, *J. Am. Chem. Soc.* **130**, 7974 (2008).
30. A. W. Ehlers, E. J. Baerends, F. M. Bickelhaupt, U. Radius, *Chem. Eur. J.* **4**, 210 (1998).
31. E. Wiberg, U. Kruerke, *Z. Naturforsch. B* **8b**, 610 (1953).
32. Materials and methods are available as supporting material on *Science* Online.
33. G. J. Irvine *et al.*, *Chem. Rev.* **98**, 2685 (1998).
34. W. Clegg *et al.*, *J. Organomet. Chem.* **550**, 183 (1998).
35. H. Braunschweig *et al.*, *Chem. Eur. J.* **13**, 7171 (2007).
36. D. L. Kays, S. Aldridge, *Struct. Bonding* **130**, 29 (2008).
37. R. C. Weast, Ed., *Handbook of Chemistry and Physics* (CRC Press, Boca Raton, FL, ed. 60, 1979).

38. This work was supported by the Deutsche Forschungsgemeinschaft. A.S. is grateful for a doctoral fellowship of the Fonds der Chemischen Industrie. Crystallographic data for compounds **2** and **3** can be obtained free of charge from the Cambridge Crystallographic Data Centre via www.ccdc.cam.ac.uk/data_request/cif, under reference nos. CCDC 758828 and 758829, respectively.

Supporting Online Material

www.sciencemag.org/cgi/content/full/328/5976/345/DC1
Materials and Methods
SOM Text
Fig. S1
References

16 December 2009; accepted 3 March 2010
10.1126/science.1186028

A Younger Age for ALH84001 and Its Geochemical Link to Shergottite Sources in Mars

T. J. Lapen,[1]* M. Righter,[1] A. D. Brandon,[1,2] V. Debaille,[3] B. L. Beard,[4,5] J. T. Shafer,[1,7] A. H. Peslier[6,8]

Martian meteorite ALH84001 (ALH) is the oldest known igneous rock from Mars and has been used to constrain its early history. Lutetium-hafnium (Lu-Hf) isotope data for ALH indicate an igneous age of 4.091 ± 0.030 billion years, nearly coeval with an interval of heavy bombardment and cessation of the martian core dynamo and magnetic field. The calculated Lu/Hf and Sm/Nd (samarium/neodymium) ratios of the ALH parental magma source indicate that it must have undergone extensive igneous processing associated with the crystallization of a deep magma ocean. This same mantle source region also produced the shergottite magmas (dated 150 to 570 million years ago), possibly indicating uniform igneous processes in Mars for nearly 4 billion years.

The orthopyroxene cumulate ALH84001 is unique in having an igneous crystallization age more than 2 billion years older than any other martian meteorite (*1*–*11*), providing critical timing constraints on the formation of Mars. Its igneous crystallization age has been difficult to determine because of its complex postcrystallization history of aqueous alteration and shock metamorphism (*12*, *13*). Although crystallization ages obtained on ALH range from 3.9 to 4.56 billion years ago (Ga) (*1*–*10*), the weighted average of Rb-Sr and Sm-Nd isotope data (*2*) yield a generally accepted age of 4.51 ± 0.11 Ga (all errors are ±2σ) (*11*). This age has important implications for the formation history of martian crust and mantle, crater chronology, and the onset of the Mars magnetic field. An age of 4.51 ± 0.11 Ga requires that a stable crust existed very early in Mars' history, not long after the onset of solar system formation at 4.568 Ga (*14*). If ALH represents crustal material formed at 4.51 Ga, then this crust must have survived a period of intense bombardment between 4.25 and 4.10 Ga (*15*, *16*), similar to the late heavy bombardment or terminal lunar cataclysm on the Moon, without suffering the intense brecciation observed in prebombardment lunar rocks. A further implication of this age is the potential presence of a magnetic field and core convection in Mars 27 to 48 million years after core formation (*17*, *18*). In order to better refine the timing of these events and to evaluate potential magmatic source affinities, we applied ^{176}Lu-^{176}Hf and ^{146,147}Sm-^{142,143}Nd chronometry to ALH.

ALH is an igneous cumulate rock that has been affected by shock-induced metamorphism and precipitation of secondary phases including carbonate and magnetite (*13*, *19*). ALH is composed of mosaic-grained orthopyroxene (~97 vol %) crystals, 4 to 5 mm in diameter, that enclose euhedral to subhedral chromite (~2 vol %) locally preserved as clasts within recrystallized granular bands. Interstitial to the mosaic-grained orthopyroxene are chromite, maskelynite, phosphate (apatite and merrillite), augite, olivine, and SiO_2 (which total ~1 vol %). The 3.6 g of ALH used in this study (sample allocations ALH84001, 365 and ALH84001, 403) have an exceptionally well-preserved igneous texture with no optical evidence of secondary phases and minimal (5 to 10 vol %) granular banding. One portion was separated into oxide (~100% chromite, sample S1) and nearly pure orthopyroxene-rich (sample S2) fractions. Two other fractions—representing the bulk rock (sample S3) and a bulk fraction after chromite removal (sample S4)—are from the disaggregated and processed material of this portion. A second portion was leached with 2.5 M HCl, resulting in a leachate-residue pair (samples L1 and R1) that was analyzed for ^{147}Sm-^{143}Nd. A third portion was crushed into a powder for high-precision ^{142}Nd/^{144}Nd analysis. Sample preparation, chemical separation, and analytical procedures are described in (*20*).

A ^{176}Lu-^{176}Hf isochron age of 4.091 ± 0.030 Ga for ALH is defined by samples S1 to S4 (Fig. 1). This age is consistent with ^{207}Pb-^{206}Pb ages of 4.074 ± 0.099 Ga (*4*) and 4.135 ± 0.012 Ga (*5*) and a U-Pb age of 4.117 ± 0.003 Ga (*5*). The Lu-Hf age is substantially younger than the respective Sm-Nd and Rb-Sr ages of 4.50 ± 0.13 Ga and 4.55 ± 0.30 Ga (*2*, *11*). The measured Lu-Hf, Pb-Pb, and U-Pb ages are similar to but slightly older than the respective Rb-Sr and Pb-Pb ages of secondary carbonate phases, 3.90 ± 0.04 Ga and 4.04 ± 0.10 Ga (*9*), as well as the U-Pb age of whitlockite and apatite, 4.018 ± 0.081 Ga (*10*). The ^{39}Ar-^{40}Ar ages of 3.92 ± 0.10 Ga and 4.1 ± 0.2 Ga (*6*, *8*) are similar to the Lu-Hf age, but shock disturbances, trapped atmospheric components, and ^{39}Ar recoil make comparisons between these isotope systems difficult. The ^{147}Sm-^{143}Nd data of samples S2 to S4 indicate an "age" of 4.405 ± 0.026 Ga, ~315 million years older than the Lu-Hf age and consistent with the previous Rb-Sr and Sm-Nd age determinations (*2*, *11*). The ^{147}Sm-^{143}Nd age of 4.889 ± 0.020 Ga defined by samples L1 and R1 is older than the age of the solar system and has an initial ^{143}Nd/^{144}Nd less than the solar system initial value (fig. S1). The counterclockwise rotation of these older isochrons requires either open-system behavior of Sm and Nd or decoupling of Sm-Nd isotope systematics during subsolidus alterations.

In ALH, 58% and 78% by weight of Sm and Nd, respectively, reside in the phosphate phases whitlockite and apatite (Table 1). The Sm-Nd apparent isochron defined by samples S2 to S4 is controlled by distribution of light rare earth element (LREE)–rich phosphates, as shown by the strong correlation (R^2 = 0.99998) between measured ^{143}Nd/^{144}Nd and Nd concentrations for each fraction (fig. S2). Because phosphates are reactive in low-pH and weathering environments, there was great potential for redistribution of Sm, Nd, and Sr in ALH resulting in spurious age and initial isotope ratios for both the Sm-Nd and Rb-Sr isotope systems. The relatively high scatter of ^{232}Th-^{208}Pb data (*5*) and a younger average U-Pb age of 4.018 ± 0.081 Ga (*10*) of apatite and whitlockite are consistent with disturbance of phosphate phases after igneous crystallization. For counterclockwise rotation of a Sm-Nd isochron, the low-Sm/Nd phase, phosphate in this case, must lose Nd relative to Sm, and the high-Sm/Nd phase orthopyroxene must have its Sm/Nd ratio decreased or unchanged. The precise mechanism of this alteration is unknown, but disturbance of the Sm-Nd system in ALH is demonstrated by the ages being too old for the leachate-residue pair coupled with a ^{143}Nd/^{144}Nd less than the solar system initial value. In contrast, orthopyroxene and chromite are the dominant Lu and Hf reservoirs (Table 1), which implies that phosphate disturbance will not affect the Lu-Hf system. Although 3% Lu resides in phosphate, its mobility would have little impact on the slope of the isochron. Because of its resistance to disturbance resulting from phosphate alteration and mutual agreement between U-Pb and Pb-Pb ages, we conclude that the Lu-Hf isochron defines the true igneous crystallization age.

The Lu-Hf age of 4.091 ± 0.030 Ga precludes it from being a remnant of primordial crust formed during solidification of an early martian magma ocean (MO). Instead, the magma that crystallized to produce ALH was derived from mantle reservoirs that have evolved isotopically since about 4.54 to 4.46 Ga (*21*). The initial ^{176}Hf/^{177}Hf of ALH cast in $\varepsilon^{176}\mathrm{Hf}_{\mathrm{CHUR}}$ notation (*22*) is –4.64 ± 1.04 (Table 2). This indicates that the ^{176}Hf/^{177}Hf of its parental magma source is less than CHUR (Fig. 2A). The calculated source ^{176}Lu/^{177}Hf—assuming a two-stage mantle evolution model (*23*), a source formation age of 4.513 Ga, a chondritic bulk Mars, and a Mars formation age of 4.567 Ga (*20*)—is 0.0183 ± 0.0036. This is similar to but substantially lower than the average source ^{176}Lu/^{177}Hf of 0.02795 ±

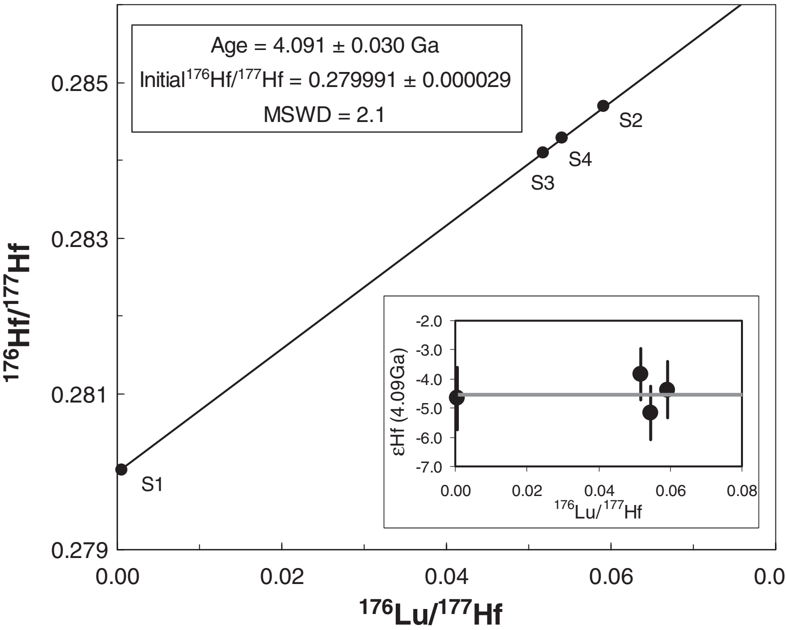

Fig. 1. Lu-Hf isochron for ALH. Inset shows Hf isotope data relative to CHUR at 4.091 Ga. Data are listed in Table 2; errors are 2σ. The isochron was calculated using IsoPlot (*34*) and a ^{176}Lu decay constant of 1.865^{-11} year^{-1} (*35*).

---

[1] Department of Earth and Atmospheric Sciences, University of Houston, Houston, TX 77204, USA. [2] NASA Johnson Space Center, Mail Code KR, Houston, TX 77058, USA. [3] Département des Sciences de la Terre et de l'Environnement, Université Libre de Bruxelles, 1050 Brussels, Belgium. [4] Department of Geosciences, University of Wisconsin, Madison, WI 53706, USA. [5] NASA Astrobiology Institute, University of Wisconsin, Madison, WI 53706, USA. [6] Jacobs Technology, Engineering and Science Contract Group, Houston, TX 77058, USA. [7] Lunar and Planetary Institute, Houston, TX 77058, USA. [8] ARES, NASA Johnson Space Center, Houston, TX 77058, USA.

*To whom correspondence should be addressed. E-mail: tjlapen@uh.edu

0.00010 (weighted mean) calculated for the distinct martian meteorite group of enriched shergottites (*24*) (Fig. 2A). The calculated source ^{147}Sm/^{144}Nd using the bulk-rock sample S3 is 0.172, slightly lower than the average source ^{147}Sm/^{144}Nd of 0.185 for the enriched shergottites (*21*). Also, the measured ^{142}Nd/^{144}Nd of ALH [ε^{142}Nd = –0.23 ± 0.05 relative to the terrestrial standard (*20*)] is slightly lower than (but within error of) the enriched shergottite average of –0.19 ± 0.05. Combined, ALH and the enriched shergottites have distinctly lower ε^{142}Nd than all other martian meteorites that have ε^{142}Nd values of –0.23 ± 0.03 to +0.65 ± 0.05 (*21*). The ALH carbonate ^{87}Sr/^{86}Sr is identical to its measured bulk rock at 3.90 ± 0.04 Ga, indicating that the carbonate Sr was primarily, if not wholly, derived from ALH (*9*). Given this, the calculated source ^{87}Rb/^{86}Sr is 0.41 to 0.35, similar to the average source of enriched shergottites of ~0.36 (*23*). Finally, similarities between ALH and enriched shergottite primary magmas are also indicated by the incompatible trace element abundances of coexisting melts with the cumulate phases in ALH (*25*). Combined, these observations indicate that ALH is derived from a source that is more incompatible trace element–enriched than shergottites. When source Sm/Nd and Lu/Hf ratios of shergottites and ALH are plotted together, they define a mixing array between hypothetical incompatible trace element–depleted and –enriched end members (Fig. 2B).

In principle, the enriched source characteristics constrained by ALH and less so by the enriched shergottites could potentially be derived from variable amounts of crustal assimilation during magma differentiation (*26*, *27*). However, from the coupled relationships between Os and Nd isotopes, shergottites cannot be related by simple mixing of depleted mantle and crust (*28*). Furthermore, crustal assimilation is not consistent with major element compositions of shergottites and their trace element and isotope systematics (*23*). From mixing calculations, the ratio of enriched component to depleted component in the martian mantle that yields the measured source ^{147}Sm/^{144}Nd and ^{176}Lu/^{177}Hf of ALH is about 0.6:0.4. Because ALH falls on the well-defined binary mixing array for Sm-Nd and Lu-Hf source compositions, it would also be highly unlikely that assimilation of mineralogically diverse crustal rocks would yield such a tight array for rocks representing parental magmas formed billions of years apart. Thus, the source for ALH was most likely in the martian mantle. This source has trace element and lithophile isotope characteristics similar but not identical to lunar KREEP (potassium–rare earth element–phosphorus) basalt sources and was likely produced by similar mechanisms (Fig. 2, A and B) (*23*, *29*).

The enriched and depleted end-member compositions in Mars likely formed from the progressive crystallization of its MO, where the residual trapped liquid components are enriched in incompatible trace elements relative to the cumulate fractions at any given point during the crystallization process (*23*, *29*–*31*) creating a hybridized mantle source with the degree of enrichment controlled by the relative proportion of trapped liquid relative to cumulate minerals. The ^{147}Sm/^{144}Nd and ^{176}Lu/^{177}Hf ratios of enriched residual liquid and depleted cumulate end-member components not only vary with degree of MO crystallization, but also with depth of equilibration and initial MO depth (Fig. 2C) (*30*). Because the modeled enriched end-member contribution to ALH parental magma is high (~60%), the composition of the enriched end

Table 1. Lu, Hf, Sm, and Nd concentrations and their calculated absolute amounts in each listed phase. See (*20*) for data reduction and analytical procedures. Modal proportions from (*19*); plagioclase and phosphate data from (*36*); orthopyroxene and chromite data from this study (*20*).

	Orthopyroxene	Chromite	Plagioclase (maskelynite)	Phosphate
Modal proportions	97%	2%	<1%	0.15%
		Element concentrations		
Lu (ppb)	48.6	0.74		900
Hf (ppb)	116.8	219.2		
Sm (ppb)	49.1		34	43,580
Nd (ppb)	73.3		378.5	179,500
		Percentage hosted in each phase		
Lu	97%	0.03%		3%
Hf	96%	4%		
Sm	42%		0.30%	58%
Nd	21%		1%	78%

Table 2. Lu-Hf and Sm-Nd isotope data measured in this study. See (*20*) for data reduction and analytical procedures.

	ALH84001, 403						ALH84001, 365
	Oxide	Pure pyroxene	Bulk rock	Dirty pyroxene	Bulk rock residue	Bulk rock leachate	Bulk rock
Sample	S1	S2	S3	S4	R1	L1	B1
Sample weight (g)	0.0127	0.0892	0.1005	0.0966	0.5052		1.01142
Lu (ppm)*	0.0007	0.0486	0.0511	0.0490			
Hf (ppm)*	0.2192	0.1168	0.1402	0.1280			
^{176}Lu/^{177}Hf*	0.0005	0.0592	0.0518	0.0545			
^{176}Hf/^{177}Hf (±2 SE)*	0.280029 ± 0.000030	0.284686 ± 0.000016	0.284116 ± 0.000011	0.284290 ± 0.000010			
$\varepsilon^{176}\text{Hf}_{(\text{today})}$ (±2 SD)	−97.12 ± 1.06	67.58 ± 0.56	47.42 ± 0.38	53.59 ± 0.37			
$\varepsilon^{176}\text{Hf}_{(4.09\ \text{Ga})}$ (±2 SD)	−4.66 ± 1.06	−3.84 ± 0.97	−4.37 ± 0.89	−5.15 ± 0.92			
$d\varepsilon^{176}\text{Hf}/d\text{Ga}$	0.32	39.08	34.21	35.97			
Sm (ppm)*		0.0562	0.1587	0.0925	0.0344	(12.57 ng)	
Nd (ppm)*		0.1003	0.5165	0.2476	0.0540	(47.71 ng)	
^{147}Sm/^{144}Nd*		0.3387	0.1857	0.2258	0.3850	0.1594	
^{143}Nd/^{144}Nd (±2 SE)*		0.516738 ± 0.000014	0.512266 ± 0.000004	0.513453 ± 0.000005	0.518544 ± 0.000008	0.511214 ± 0.000005	0.513226 ± 0.000002
$\varepsilon^{143}\text{Nd}_{(\text{today})}$ (±2 SD)		80.00 ± 0.28	−7.24 ± 0.08	15.92 ± 0.09	115.23 ± 0.15	−27.76 ± 0.09	
$\varepsilon^{143}\text{Nd}_{(4.09\ \text{Ga})}$ (±2 SD)		4.79 ± 0.38	−1.60 ± 0.21	0.37 ± 0.25	15.61 ± 0.43	−8.29 ± 0.18	
ε^{142}Nd (±2 SE)							−0.23 ± 0.05

*Concentrations and isotope ratios are corrected for the following blank values: 18 pg Lu; 80 pg Hf with ^{176}Hf/^{177}Hf = 0.2822; 20 pg Sm; and 50 pg Nd with ^{143}Nd/^{144}Nd = 0.5116.

member is nearly identical to its calculated source composition. The enriched component likely represents deep (200 to 750 km) residual trapped liquid (RTL) equilibrated with cumulates after ~93% MO crystallization (*30*) (Fig. 2C). This component is unlike that derived from shallow, very late-stage liquids remaining after >98% MO crystallization that explains lunar KREEP (*31*) (Fig. 2C). Additionally, cumulates in equilibrium with this RTL are a good match for the composition of the depleted mantle end-member composition as evidenced by shergottite source modeling (*30*) and our finding that mixtures of these two components can generate the observed sources of shergottites and ALH that range in age from 0.165 to 4.091 Ga (Fig. 2B). Therefore, it is likely that similar magmatic source regions in Mars that produced the long-lived Tharsus and Elysium volcanic regions have been producing magmas for at least the past 4 billion years.

The igneous crystallization of ALH occurred at 4.091 ± 0.030 Ga, during a period of intense bombardment and slightly prior to cessation of the Mars global magnetic field (*15*, *16*, *32*). As such, the magnetic properties of the igneous phases in ALH (*17*) do not record early planetary magnetic fields, as implied for a crystallization age of ~4.5 Ga, and must instead reflect conditions after accretion and ~400 million years of cooling in Mars. The Lu-Hf age requires a much shorter time interval between igneous formation and aqueous alteration at 4.04 ± 0.10 to 3.90 ± 0.04 Ga, necessitating a revision of the timing of pre-alteration textures (*13*). The younger age predicts that the primordial martian crust was likely largely destroyed from intense bombardment at 4.25 to 4.1 Ga (*15*).

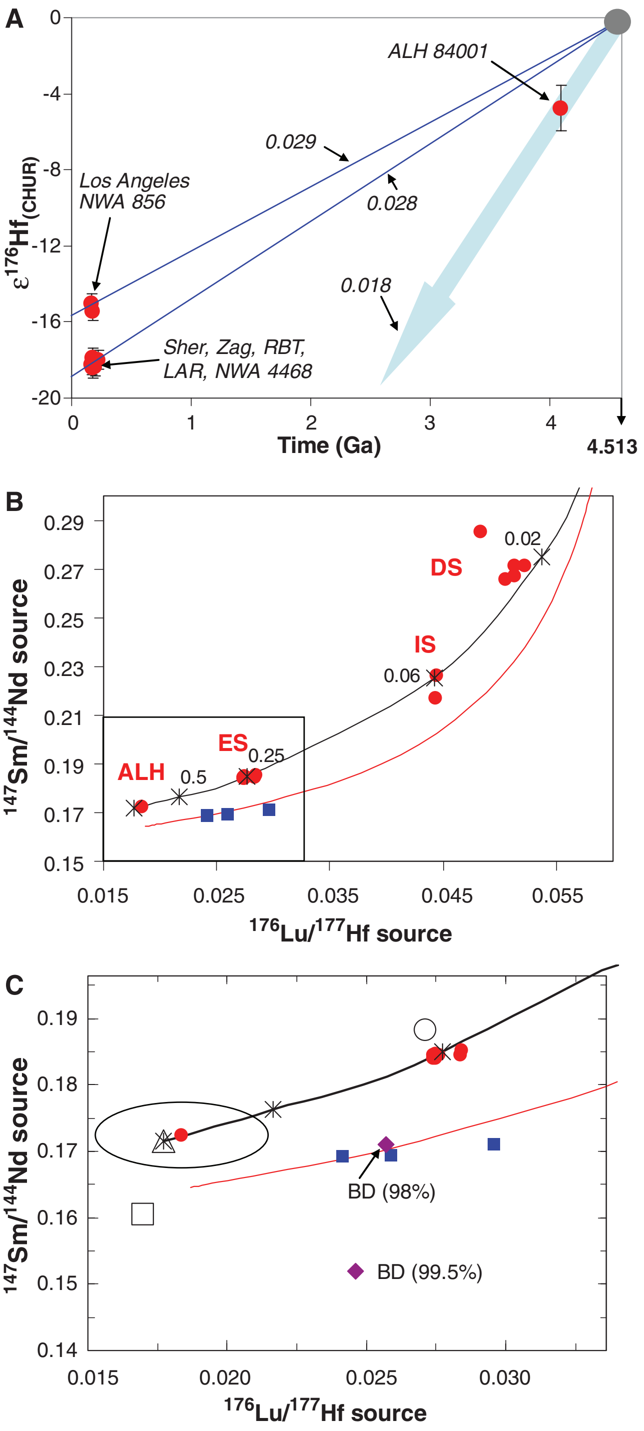

Fig. 2. (**A**) Hf isotope evolution diagram relative to CHUR (*33*) of sources for enriched shergottites RBT 04262 (RBT), NWA 4468, Shergotty (Sher), Zagami (Zag), LAR 06319 (LAR), Los Angeles, and NWA 856 (*24*, *30*, *37*–*40*) as well as ALH. There are different recent interpretations of the ages of the shergottites. We have calculated all of the source ^{176}Lu/^{177}Hf and ^{147}Sm/^{144}Nd ratios of shergottites assuming that their igneous crystallization ages are given by their internal isochron ages (0.15 to 0.57 Ga) (*11*, *23*, *24*, *29*, *38*–*40*), not their older Pb-Pb ages (~4.1 Ga) (*4*, *38*, *39*); see (*20*) for further discussion. The isotopic evolution of the sources for the plotted samples is based on a two-stage model (*23*, *29*) where the sources formed from a chondritic reservoir at 4.513 Ga. The ^{176}Lu/^{177}Hf source values are indicated by the numbers referencing the isotopic evolution lines. (**B**) Mixing diagram for shergottites and ALH ^{147}Sm/^{144}Nd and ^{176}Lu/^{177}Hf source compositions. Red dots, shergottites; DS, depleted shergottites DaG 476, QUE 94201, SaU 094, DaG 476, and SaU 008; IS, intermediate shergottites EETA 79001 and ALH 77005; ES, enriched shergottites RBT 04262, LAR 06319, Shergotty, Zagami, NWA 4468, NWA 856, and Los Angeles; ALH, ALH 84001. The black binary mixing line is based on source compositions of residual trapped liquid (RTL) and cumulates in the upper mantle assemblage (UM1) of (*30*) produced in MO 2000 to 1350 km deep. The red mixing line was calculated with source end-member compositions used in (*23*). Blue squares are calculated sources for KREEP-rich lunar basalts. Isotope data used for the source calculations of shergottites come from (*21*, *23*, *24*, *29*, *30*, *37*–*40*). Labeled mixing proportions (black symbols) are based on the fractions of RTL. (**C**) Enlargement of boxed area of (B). Solid symbols are defined as in (B) and represent calculated source compositions; open symbols represent the ^{147}Sm/^{144}Nd and ^{176}Lu/^{177}Hf compositions of liquid in equilibrium with cumulates during MO crystallization (*30*). For MO 2000 to 1350 km deep, the open square represents RTL in the shallow upper mantle after 98% MO crystallization, the open triangle represents RTL in the upper mantle [UM1 of (*30*)] after 90 to 94% crystallization, and the open circle is RTL in the upper mantle [UM2 of (*30*)] after ~66% crystallization. Enriched end-member compositions (*31*) are labeled BD; percent values represent degree of MO crystallization. Ellipse reflects 2σ error of calculated source compositions for ALH.

References and Notes

1. E. Jagoutz, A. Sorowka, J. D. Vogel, H. Wanke, *Meteoritics* **29**, 478 (1994).
2. L. E. Nyquist, B. M. Bansal, H. Wiesmann, C.-Y. Shih, *Lunar Planet. Sci. Conf.* **26**, 1065 (1995).
3. M. Wadhwa, G. Lugmair, *Meteorit. Planet. Sci.* **31**, A145 (1996).
4. A. Bouvier, J. Blichert-Toft, F. Albarède, *Earth Planet. Sci. Lett.* **280**, 285 (2009).
5. E. Jagoutz *et al.*, *Lunar Planet. Sci. Conf.* **40**, 1662 (2009).
6. G. Turner, S. F. Knott, R. D. Ash, J. D. Gilmour, *Geochim. Cosmochim. Acta* **61**, 3835 (1997).
7. S. Ilg *et al.*, *Meteorit. Planet. Sci.* **32**, A65 (1997).
8. D. D. Bogard, D. H. Garrison, *Meteorit. Planet. Sci.* **34**, 451 (1999).
9. L. E. Borg *et al.*, *Science* **286**, 90 (1999).
10. K. Terada, T. Monde, Y. Sano, *Meteorit. Planet. Sci.* **38**, 1697 (2003).
11. L. E. Nyquist *et al.*, *Space Sci. Rev.* **96**, 105 (2001).
12. K. L. Thomas-Keprta, S. J. Clemett, D. S. McKay, E. K. Gibson, S. J. Wentworth, *Geochim. Cosmochim. Acta* **73**, 6631 (2009).
13. A. H. Treiman, *Meteorit. Planet. Sci.* **33**, 753 (1998).
14. A. Bouvier, J. Blichert-Toft, F. Moynier, J. Vervoort, F. Albarede, *Geochim. Cosmochim. Acta* **71**, 1583 (2007).
15. H. V. Frey, *Geophys. Res. Lett.* **35**, L13203 (2008).
16. R. J. Lillis, H. V. Frey, M. Manga, *Geophys. Res. Lett.* **35**, L14203 (2008).
17. B. P. Weiss *et al.*, *Earth Planet. Sci. Lett.* **201**, 449 (2002).
18. T. Kleine *et al.*, *Geochim. Cosmochim. Acta* **73**, 5150 (2009).
19. C. Meyer, Mars meteorite compendium, NASA-ARES JSC #27672 Revision C (2008).

20. See supporting material on *Science* Online.
21. V. Debaille, A. D. Brandon, Q. Z. Yin, B. Jacobsen, *Nature* **450**, 525 (2007).
22. $\varepsilon^{176}Hf_{CHUR} = (^{176}Hf/^{177}Hf_{CHUR}/^{176}Hf/^{177}Hf_{CHUR} - 1) \times 10{,}000$; CHUR refers to chondritic uniform reservoir model values for the Lu-Hf, as well as Sm-Nd, isotope systems. Hf and Nd CHUR reference values are from (*33*) and references therein.
23. L. E. Borg *et al.*, *Geochim. Cosmochim. Acta* **67**, 3519 (2003).
24. T. J. Lapen *et al.*, *Lunar Planet. Sci. Conf.* **40**, 2376 (2009).
25. J. A. Barrat, C. Bollinger, *Meteorit. Planet. Sci.* **44** (suppl.), abstr. 5106 (2009) (www.lpi.usra.edu/meetings/metsoc2009/pdf/5106.pdf).
26. J. H. Jones, *Lunar Planet. Sci. Conf.* **19**, 465 (1989).
27. D. Rumble, A. J. Irving, *Lunar Planet. Sci. Conf.* **40**, 2293 (2009).
28. A. D. Brandon *et al.*, *Geochim. Cosmochim. Acta* **64**, 4083 (2000).
29. L. E. Borg *et al.*, *Geochim. Cosmochim. Acta* **61**, 4915 (1997).
30. V. Debaille, Q.-Z. Yin, A. D. Brandon, B. Jacobsen, *Earth Planet. Sci. Lett.* **269**, 186 (2008).
31. L. E. Borg, D. S. Draper, *Meteorit. Planet. Sci.* **38**, 1713 (2003).
32. J. H. Roberts, R. J. Lillis, M. Manga, *J. Geophys. Res.* **114**, (E4), E04009 (2009).
33. A. Bouvier, J. Vervoort, P. Patchett, *Earth Planet. Sci. Lett.* **273**, 48 (2008).
34. K. R. Ludwig, *Berkleley Geochronology Center Spec. Pub. 1a*, 59 (2003).
35. E. E. Scherer, C. Münker, K. Mezger, *Science* **293**, 683 (2001).
36. M. Wadhwa, G. Crozaz, *Meteorit. Planet. Sci.* **33**, 1713 (1998).
37. J. Blichert-Toft *et al.*, *Earth Planet. Sci. Lett.* **173**, 25 (1999).
38. A. Bouvier, J. Blichert-Toft, J. D. Vervoort, F. Albarède, *Earth Planet. Sci. Lett.* **240**, 221 (2005).
39. A. Bouvier, J. Blichert-Toft, J. D. Vervoort, P. Gillet, F. Albarède, *Earth Planet. Sci. Lett.* **266**, 105 (2008).
40. C.-Y. Shih, L. E. Nyquist, Y. Reese, *Lunar Planet. Sci. Conf.* **40**, 1360 (2009).

41. Supported by NASA Cosmochemistry grants (T.J.L. and A.D.B.), a NASA Astrobiology grant (B.L.B.), the University of Houston Institute for Space Systems Operations (T.J.L.), and the Belgian Fund for Scientific Research (V.D.). We thank three anonymous reviewers for improving the clarity of the manuscript.

Supporting Online Material

www.sciencemag.org/cgi/content/full/328/5976/347/DC1
Materials and Methods
Figs. S1 to S5
References

1 December 2009; accepted 3 March 2010
10.1126/science.1185395

Evolution of an Expanded Sex-Determining Locus in *Volvox*

Patrick Ferris,[1]* Bradley J. S. C. Olson,[1]* Peter L. De Hoff,[1] Stephen Douglass,[2] David Casero,[2] Simon Prochnik,[3] Sa Geng,[1] Rhitu Rai,[1,4] Jane Grimwood,[5] Jeremy Schmutz,[5] Ichiro Nishii,[6] Takashi Hamaji,[7] Hisayoshi Nozaki,[7] Matteo Pellegrini,[2] James G. Umen[1]†

Although dimorphic sexes have evolved repeatedly in multicellular eukaryotes, their origins are unknown. The mating locus (*MT*) of the sexually dimorphic multicellular green alga *Volvox carteri* specifies the production of eggs and sperm and has undergone a remarkable expansion and divergence relative to *MT* from *Chlamydomonas reinhardtii*, which is a closely related unicellular species that has equal-sized gametes. Transcriptome analysis revealed a rewired gametic expression program for *Volvox MT* genes relative to *Chlamydomonas* and identified multiple gender-specific and sex-regulated transcripts. The retinoblastoma tumor suppressor homolog *MAT3* is a *Volvox MT* gene that displays sexually regulated alternative splicing and evidence of gender-specific selection, both of which are indicative of cooption into the sexual cycle. Thus, sex-determining loci affect the evolution of both sex-related and non–sex-related genes.

Sexually dimorphic gametes have evolved in every major group of eukaryotes, and are thought to be selected when parents can differentially allocate resources to progeny (*1*). However, the origins of oogamy (large eggs and small sperm) and the contribution of sex-determining loci to such evolution are largely unknown (*2*, *3*) [see the glossary of terms (*4*) for further explanation of terminology].

The Volvocine algae are a group of chlorophytes comprising unicellular species, such as *Chlamydomonas reinhardtii* (hereafter *Chlamydomonas*), and a range of multicellular species of varying complexity, such as *Volvox carteri* (hereafter *Volvox*). *Volvox* has a vegetative reproductive form containing 16 large germ cells (gonidia) and ~2000 terminally differentiated somatic cells (fig. S1) (*4*, *5*).

Chlamydomonas and other Volvocine algae also undergo a sexual cycle in which a large, haploid mating locus (*MT*) controls sexual differentiation, mating compatibility, and zygote development (*6*). *MT* in *Chlamydomonas* is a 200- to 300-kb multigenic chromosomal region (Fig. 1A) within which gene order is rearranged between the two sexes (*MT*+ and *MT*–) and meiotic recombination is suppressed, thus leading to its inheritance as a single Mendelian trait. Within each *MT* allele are gender-limited genes (allele present in only one of the two sexes), which are required for the sexual cycle, as well as shared genes (alleles present in both sexes), most of which have no known function in sex or mating (*7*). The rearrangements that suppress recombination serve to maintain linkage of gender-limited genes, but they also reduce genetic exchange between shared genes, leading to their meiotic isolation. Thus, *Chlamydomonas MT* bears similarity to sex chromosomes and to expanded mating-type regions of some fungi and bryophytes (*8*–*10*).

Although *Chlamydomonas* is isogamous (producing equal-sized gametes), *Volvox* and several other Volvocine genera have evolved oogamy that is under the control of female and male *MT* loci (fig. S1) (*11*). Moreover, the *Volvox* sexual cycle is characterized by a suite of other traits not found in *Chlamydomonas*, such as a diffusible sex-inducer protein rather than nitrogen deprivation (–N) as a trigger for gametogenesis (table S1). A detailed characterization of *MT* in *Volvox* would be expected to shed light on the transition from isogamy to oogamy and on other properties of the sexual cycle that evolved in this multicellular species (table S1).

The *MT*+ allele of *Chlamydomonas* was previously sequenced and resides on chromosome 6 (Fig. 1A and fig. S2) (*12*). To enable a comparison of mating loci evolution between two related species with markedly different sexual cycles, we sequenced *Chlamydomonas MT*– and both alleles of *Volvox MT* (Fig. 1 and table S2) (*4*). *Volvox MT* was previously assigned to linkage group I (LG I) (*5*), but the locus had not been further characterized. We mapped *Volvox MT* to the genome sequence and assembled most of LG I (table S3) (*4*). Extensive synteny with *Chlamydomonas* chromosome 6 indicates that *MT* has remained on the same chromosome in both lineages for ~200 million years since their estimated divergence, despite numerous intrachromosomal rearrangements between the two (fig. S2) (*13*).

Although the haploid *Volvox* genome is ~17% larger than that of *Chlamydomonas* (138 Mb versus 118 Mb) and the two have very similar predicted proteomes (*12*, *14*), *Volvox MT* is ~500% larger than *Chlamydomonas MT* and contains over 70 protein-coding genes in each allele (Fig. 1B and tables S4 and S5). Compared with autosomes, *Volvox MT* is unusually repeat-rich (greater than three times the genomic average), has lower gene density, and has genes with more intronic sequence (table S6), all of which are properties that suggest an unusual evolutionary history and distinguish it from *Chlamydomonas MT*.

Only two gender-limited genes from *Chlamydomonas MT*–, *MID* and *MTD1*, have recognizable homologs in *Volvox* that are both in male *MT*

---

[1] The Salk Institute for Biological Studies, La Jolla, CA 92037, USA. [2] Institute for Genomics and Proteomics and Department of Molecular, Cell and Developmental Biology, University of California, Los Angeles, CA 90095, USA. [3] U.S. Department of Energy (DOE) Joint Genome Institute (JGI), Walnut Creek, CA 95498, USA. [4] Laboratory of Plant Microbe Interaction, National Research Center on Plant Biotechnology, Pusa Campus, Indian Agricultural Research Institute, New Delhi 110012, India. [5] Genome Sequencing Center, Hudson Alpha Institute for Biotechnology, Huntsville, AL 35806, USA. [6] Department of Biological Science, Nara Women's University, Nara 630-8506, Japan. [7] Department of Biological Sciences, University of Tokyo, Tokyo 113-0033, Japan.

*These authors contributed equally to this work.

†To whom correspondence should be addressed. E-mail: umen@salk.edu